AGU PUBLICATIONS

Geophysical Research Letters

RESEARCH LETTER
10.1002/2013GL058742

Key Points:
- Full-wave effects lead to complexities in splitting intensity
- Our method widens the range of source-receiver geometry in splitting analysis
- Full-wave kernels enable 3-D imaging of anisotropy structures

Correspondence to:
Y.-P. Lin,
f97224204@ntu.edu.tw

Citation:
Lin, Y.-P., L. Zhao, and S.-H. Hung (2014), Full-wave effects on shear wave splitting, *Geophys. Res. Lett.*, *41*, 799–804, doi:10.1002/2013GL058742.

Received 16 NOV 2013
Accepted 3 JAN 2014
Accepted article online 6 JAN 2014
Published online 4 FEB 2014

Full-wave effects on shear wave splitting

Yu-Pin Lin[1], Li Zhao[2], and Shu-Huei Hung[1]

[1]Department of Geosciences, National Taiwan University, Taipei, Taiwan, [2]Institute of Earth Sciences, Academia Sinica, Taipei, Taiwan

Abstract Seismic anisotropy in the mantle plays an important role in our understanding of the Earth's internal dynamics, and shear wave splitting has always been a key observable in the investigation of seismic anisotropy. To date the interpretation of shear wave splitting in terms of anisotropy has been largely based on ray-theoretical modeling of a single vertically incident plane SKS or SKKS wave. In this study, we use sensitivity kernels of shear wave splitting to anisotropic parameters calculated by the normal-mode theory to demonstrate that the interference of SKS with other phases of similar arrival times, near-field effect, and multiple reflections in the crust lead to significant variations of SKS splitting with epicentral distance. The full-wave kernels not only widen the possibilities in the source-receiver geometry in making shear wave splitting measurements but also provide the capability for tomographic inversion to resolve vertical and lateral variations in the anisotropic structures.

1. Introduction

Knowledge on the Earth's anisotropic structure allows us to characterize the deformation and the dynamic processes in the Earth's interior. Shear wave splitting has been an important observable in the investigation of elastic anisotropy in the crust and upper mantle. Up to the recent past, the interpretation of shear wave (SKS and/or SKKS) splitting in terms of anisotropy has primarily relied on ray theory under the approximation of a single plane shear wave with nearly vertical incidence angle. Under this scenario, all shear wave splitting measurements at a given station are reduced to two apparent anisotropy parameters: the splitting time δt between fast and slow quasi-shear waves and the azimuth ϕ_f of the fast axis (the polarization of the fast quasi-shear wave), through a sinusoidal relation:

$$S_i = \delta t \sin 2\left(\phi_f - \phi_b^i\right), \tag{1}$$

where S_i is the shear wave splitting measurement at the ith station whose back-azimuth is ϕ_b^i. The pair of apparent anisotropy parameters then prescribes a uniform layer of anisotropy beneath the station, and the amount of splitting varies with the differential angle $\phi_f - \phi_b^i$ only.

The simple relation in equation (1) provides a clear and practical approach to the interpretation of shear wave splitting measurements, and it has been widely applied in studying upper mantle anisotropy [e.g., *Ando*, 1984; *Vinnik et al.*, 1984; *Silver and Chan*, 1988; *Silver*, 1996; *Savage*, 1999; *Wüstefeld et al.*, 2008]. However, the assumption of a vertically incident plane wave precludes the resolution of the spatial variation of anisotropy by shear wave splitting, and the requirement of a single (i.e., isolated) SKS or SKKS wave severely limits the source-station geometry amenable for making splitting measurements.

Chevrot [2000] demonstrated that the optimal measurement of shear wave splitting in equation (1), which has since been referred to as the *splitting intensity* (SI), can be obtained by projecting the transverse-component signal onto the time derivative of the radial-component signal. That recognition enabled *Favier and Chevrot* [2003] and *Favier et al.* [2004] to derive the expression for the three-dimensional (3-D) sensitivity (Fréchet) kernels of the SI to elastic anisotropic structural parameters. These 3-D kernels for the SI were later used by *Monteiller and Chevrot* [2011] to image the crust and upper-mantle anisotropy in southern California. *Sieminski et al.* [2008] examined the 3-D kernels for the SI using the accurate but numerically demanding adjoint spectral-element method [*Tromp et al.*, 2005; *Liu and Tromp*, 2006], and pointed out the neglected dependence on the incidence angle of SKS wave in the 3-D sensitivity kernels of *Favier and Chevrot* [2003] and *Favier et al.* [2004]. It should be pointed out, however, that *Chevrot* [2006] has extended their 3-D sensitivity kernels to the case of nonvertically incident SKS waves.

In this study, we adopt the more efficient approach of *Zhao and Chevrot* [2011a, 2011b] for calculating full-wave Fréchet kernels to conduct a thorough and detailed investigation on the 3-D sensitivity of the SI to

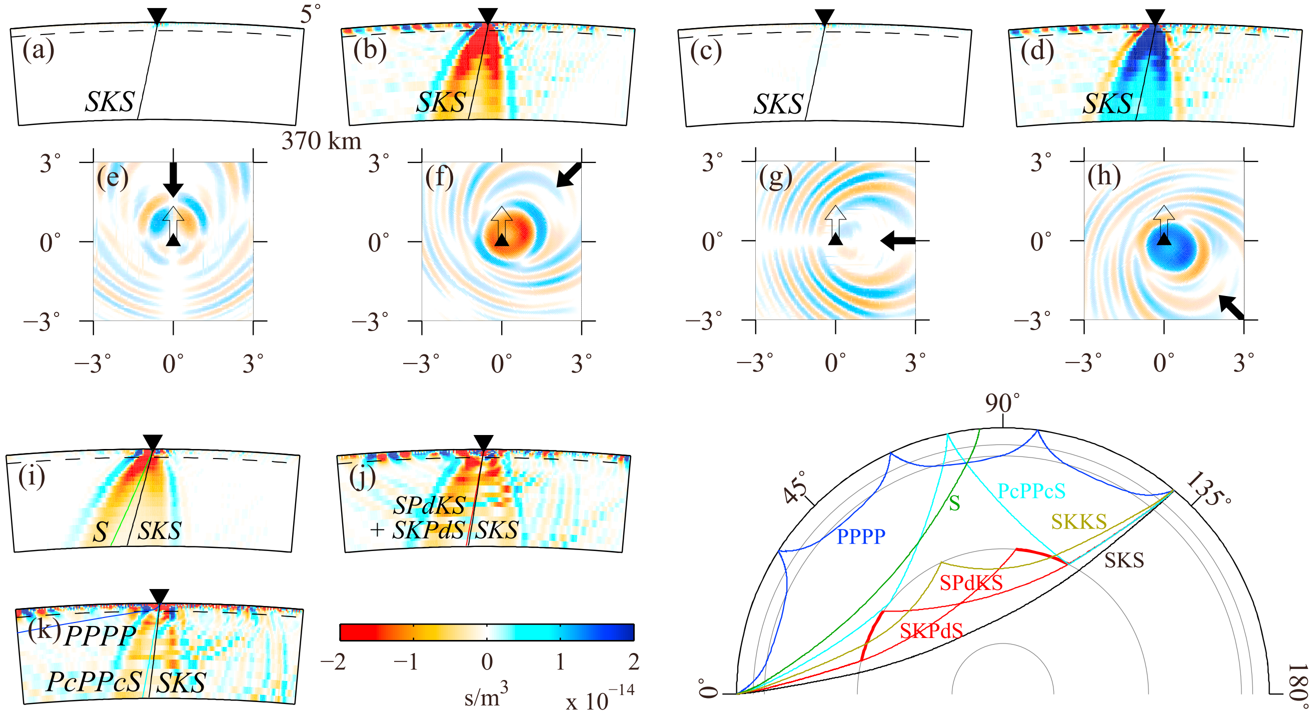

Figure 1. Full-wave Fréchet kernels of the splitting intensity SI for shear wave anisotropy parameter γ with different source-receiver geometries. These are sensitivities of the SI of the signals in the SKS time window (shaded region in Figure 2b) to γ. The source is always at the surface. The kernels are shown (a–d and i–k) in the source-receiver great-circle plane and (e–h) in map view at 200 km depth. In all examples, the fast axis of anisotropy is north-south, i.e., $\phi_f = 0°$, shown by the open arrows in map view plots (Figures 1e–1h). The paired plots (Figures 1a and 1e, 1b and 1f, 1c and 1g, and 1d and 1h) correspond to the incident shear waves at the same epicentral distance of 100° but different back-azimuths ϕ_b of 0°, 45°, 90°, and 135°, respectively, shown by the black arrows in map view plots (Figures 1e–1h). The kernels for the back-azimuths of 0° (Figures 1a and 1e) and 90° (Figures 1c and 1g) are weak with negligible integrated sensitivities, whereas those for the back-azimuths of 45° (Figures 1b and 1f) and 135° (Figures 1d and 1h) are strong with opposite signs. In Figures 1i–1k, the epicentral distances are 85°, 115°, and 130°, respectively, while the back-azimuths are all 45°. At these distances, the kernels are more complex due to stronger interference of SKS with other phases. Raypaths for the relevant phases are shown in the bottom right plot.

anisotropic structure. We demonstrate that the SI measurements at a given station are affected by not only the back-azimuth of the SKS wave, but also its incidence angle due to variations in epicentral distance and source depth, and the interference between the SKS wave and neighboring phases. As a result, our full-wave kernels enable us to conduct 3-D tomography inversions of the anisotropic structure using the SI measurements obtained from a much wider range of source-station geometry.

2. Full-Wave Sensitivity of Splitting Intensity to Anisotropy

As shown in *Chevrot* [2000], the SI measured at a station with recorded radial- and transverse-component signals $u_R(t)$ and $u_T(t)$, respectively, can be expressed as [e.g., *Favier and Chevrot*, 2003; *Chevrot*, 2006; *Sieminski et al.*, 2008]:

$$S = -2\frac{\int_{t_1}^{t_2} \dot{u}_R(t)u_T(t)\mathrm{d}t}{\int_{t_1}^{t_2} [\dot{u}_R(t)]^2\mathrm{d}t}, \tag{2}$$

where the integrals are taken over the time window $[t_1, t_2]$ selected for each shear wave phase of interest and the dot above $u_R(t)$ indicates its time derivative. The interpretation or modeling of the SI data in terms of anisotropy is enabled by the so-called sensitivity or Fréchet kernels through the integral relationship

$$S = \int_0^a \left\{ \int_0^{2\pi}\int_0^{\pi} \left[K_\varepsilon^S(r,\theta,\varphi)\varepsilon(r,\theta,\varphi) + K_\delta^S(r,\theta,\varphi)\delta(r,\theta,\varphi) + K_\gamma^S(r,\theta,\varphi)\gamma(r,\theta,\varphi) \right] r^2 \sin\theta d\theta d\varphi \right\} dr, \tag{3}$$

where (r, θ, φ) is an arbitrary location in the Earth of radius a. $\varepsilon = (C_{11} - C_{33})/2\rho\alpha^2$, $\delta = (C_{13} - C_{33} + 2C_{44})/\rho\alpha^2$, and $\gamma = (C_{66} - C_{44})/2\rho\beta^2$ are dimensionless anisotropy parameters [*Mensch and Rasolofosaon*, 1997; *Becker et al.*, 2006; *Chevrot*, 2006]. Here ρ is density, α and β are, respectively, the isotropic *P* and *S* wave velocities

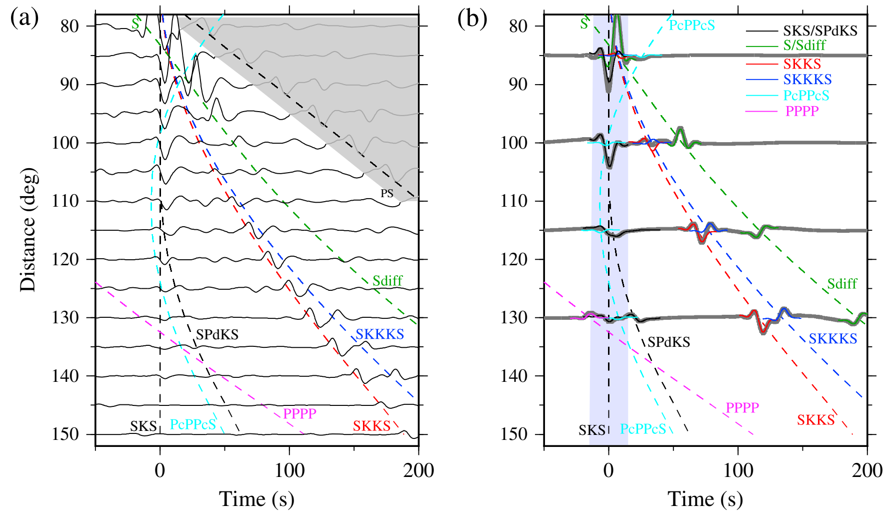

Figure 2. (a) Synthetic seismograms calculated by normal-mode summations in 1-D model PREM for epicentral distances between 80° and 150° with an interval of 5°. The sources are all at the surface. All waveforms have been band-pass filtered between 0.008 Hz and 0.12 Hz, and are aligned at $t = 0$ by the predicted SKS arrival times. To avoid distraction by the large-amplitude surface waves, the amplitudes of the waveforms in the shaded zone have been divided by the factor $3\Delta^2$, where Δ is the epicentral distance. (b) Synthetics for individual phases (thin lines) calculated by the WKBJ method [*Chapman et al.*, 1988] at the distances of 85°, 100°, 115°, and 130°. Thick lines are the summation of the individual waveforms. Shaded zone indicates the SKS time window [t_1, t_2] used in the calculation of the kernels in Figure 1. Thin dashed lines in Figures 2a and 2b are traveltime curves for model PREM calculated by the TauP Toolkit [*Crotwell et al.*, 1999].

in the reference model, and C_{ij} are the elements of the elasticity tensor in the Voigt notation [*Babuška and Cara*, 1991; *Browaeys and Chevrot*, 2004].

Equation (2) tells us how the SI is measured from radial- and transverse-component waveforms. The expression is remarkably similar to that for a finite-frequency traveltime shift (delay) between recorded and synthetic seismograms measured by their cross correlation [e.g., *Zhao and Jordan*, 1998, equation (18); *Dahlen et al.*, 2000, equation (66)]. This suggests an alternative interpretation of the causal effect between anisotropy structure and the SI, analogous to that between velocity perturbation and delay time: The transverse-component signal $u_T(t)$ can be viewed as energy scattered from the radial-component signal $u_R(t)$ by anisotropy parameters ε, δ, and γ, and the SI is merely the finite-frequency delay time of $u_T(t)$ relative to $u_R(t)$. Therefore, we can expect to see the SI kernels displaying the banana-doughnut features similar to the finite-frequency traveltime kernels with zero sensitivity along the raypath [e.g., *Dahlen et al.*, 2000; *Zhao et al.* 2000].

Zhao and Chevrot [2011a, 2011b] proposed the expressions for the Fréchet kernels of widely used observables in seismic tomography with respect to various of model parameters in terms of the strain Green tensors (SGT). That approach affords both efficiency and flexibility in the calculation of full-wave Fréchet kernels with the help of SGT databases obtained by accurate wavefield modeling algorithms such as the normal-mode theory for one-dimensional (1-D) models or numerical simulations for 3-D models. Figure 1 shows the 3-D SI kernels for γ with several source-receiver geometries for the Preliminary Reference Earth Model (PREM) [*Dziewonski and Anderson*, 1981]. The spatial pattern of the SI sensitivity to γ changes dramatically with back-azimuth and epicentral distance. For instance, the pattern of the SKS kernel at 100° distance for different azimuths (Figures 1a–1h) is similar to that predicted by ray theory, i.e., a simple sinusoidal variation with the differential angle $\phi_f - \phi_b$ as in equation (1). Synthetic seismogram calculated for the same distance (Figure 2) indicates that SKS is the dominant phase arriving in the estimated SKS window (shaded zone in Figure 2b). Thus, all the kernels in Figures 1a–1h display a single, simple banana-doughnut shape. At distances of 85°, 115°, and 130°, however, the sensitivities for the signals in the SKS window are more complex due to increased interference with other phases. At the distance of 85°, a strong mantle-turning *S* wave (green line in Figure 2b) arrives right at the tail of SKS, making the separation of the two phases impossible. This leads to the broadening of the calculated kernel shown in Figure 1i. At 115°, the phases SPdKS/SKPdS with diffractions along the core-mantle boundary (CMB) and the twice CMB-reflected PcPPcS arrive closely in time to a relatively weak SKS, leading to a stronger interference effect and a more chaotic pattern in the kernel (Figure 1j). Similarly at 130°, contribution from the surface-reflected PPPP

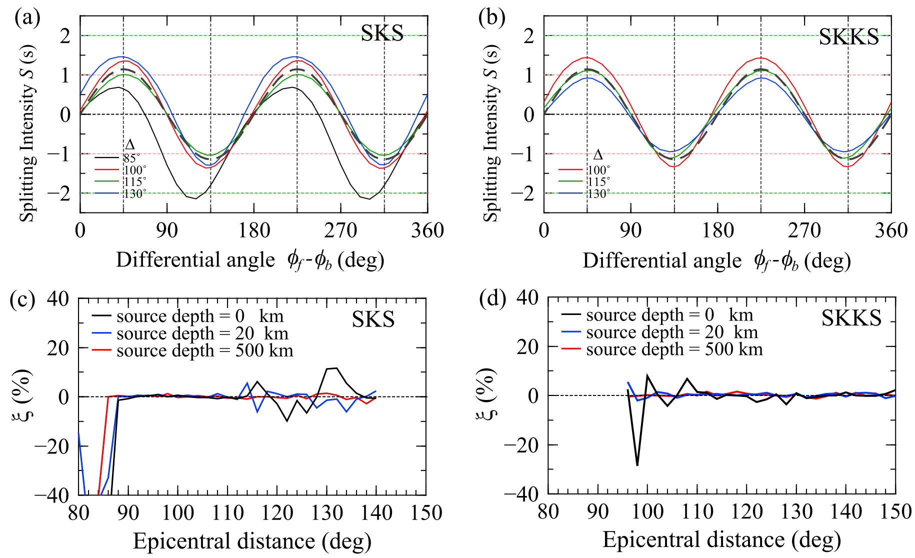

Figure 3. (a) Splitting intensity predictions of SKS as functions of the differential angle $\phi_f - \phi_b$ assuming a uniform anisotropy of $\gamma = -0.02$, $\varepsilon = -0.0189$, and $\delta = -0.0096$ in the top 250 km layer. Solid lines show predictions by the full-wave 3-D kernels for surface sources at four epicentral distances (black: 85°; red: 100°; green: 115°; blue: 130°). The dashed line is the prediction by the simple relation $S = \delta t \sin 2(\phi_f - \phi_b)$, where $\delta t = 1.15$ s, corresponding to $\gamma = -0.02$. (b) Same as Figure 3a but for SKKS at epicentral distances of 100°, 115°, and 130°. Variations of the shifting parameter ξ defined in equation (4) with distance for (c) the SKS time window, and (d) the SKKS time window. Black, blue, and red lines are for source depths at 0 km, 20 km and 500 km, respectively.

makes the kernel even more complicated (Figure 1k). The effect of these interferences can be seen more clearly when we integrate these 3-D kernels for a suite of differential angles $\phi_f - \phi_b$ and compare with the simple relation predicted by equation (1).

3. Full-Wave Effects on SKS Splitting Intensity

As discussed earlier, the simple sinusoidal dependence of the SI on the differential angle $\phi_f - \phi_b$ in equation (1) is based on the assumption of a single vertically incident plane SKS wave. Therefore, its validity hinges on whether the SKS phase in the time window for measuring the SI is contaminated by other phases. The waveforms in Figure 2b suggest that in the distance ranges of 80°–90° and 110°–130° SKS may be affected by other phases. To quantify the interference effect on the SKS splitting intensity, we integrate the 3-D sensitivity kernels assuming a uniform anisotropy of $\gamma = -0.02$ in the top 250 km depth range for a suite of differential angles $\phi_f - \phi_b$ and compare them with those predicted by the ray-theoretical relation in equation (1). The result is shown in Figure 3. In obtaining the full-wave SI predictions, contributions from ε and δ are accounted for by adopting the scaling relations among the anisotropy parameters [*Becker et al.*, 2006], i.e., $\varepsilon = -0.0189$ and $\delta = -0.0096$. *Zhao and Chevrot* [2011b] showed that the sensitivity kernels of the SI for ε and δ are approximately an order of magnitude smaller than that for γ. As a result, the contributions to the SI predictions by ε and δ amount to only 4% and 9.5% of that by γ, respectively.

The prediction of $S = \delta t \sin 2(\phi_f - \phi_b)$ for a single plane SKS or SKKS wave with vertical incidence is a simple sinusoid (black dashed lines in Figures 3a and 3b), reaching peak values of $\pm\delta t$ at the differential angles 90°∓45° and 270°∓45°. The predictions from the 3-D kernels, however, are quite different depending on the epicentral distance. These 3-D kernels are calculated by the accurate normal-mode theory which fully accounts for the interference of all possible waves arriving in the time window used to measure the SI. Also included in these full-wave 3-D kernels but neglected in ray theory are the near-field effect in the vicinity of stations and the complex wavefield interactions with near-surface discontinuities.

Since the ray-theoretical curve (dashed sinusoids in Figures 3a and 3b) has a zero mean, we can use the vertical shifts of the other curves to assess the full-wave effect on the SI predictions. Thus, for a given prediction curve we define a shifting parameter

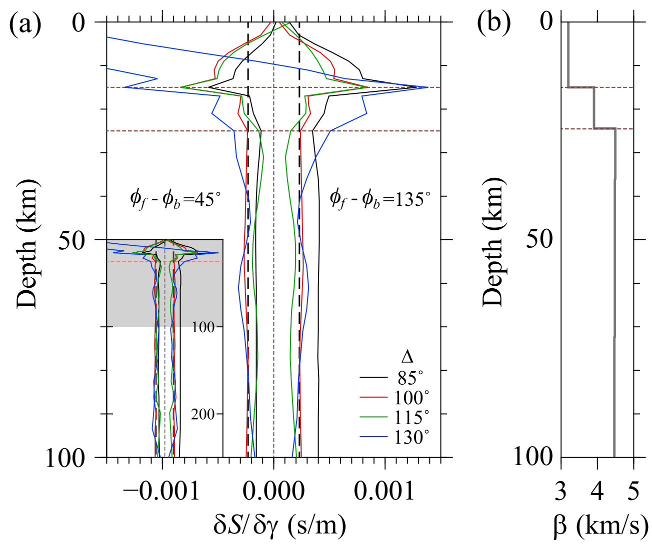

Figure 4. (a) Depth variations of horizontally integrated 3-D splitting intensity kernels. Kernels for different epicentral distances are depicted by lines of different colors (black: 85°; red: 100°; green: 115°; blue: 130°). All kernels are calculated using two values of the differential angle $\phi_f - \phi_b$. The kernels having negative amplitudes in the mantle correspond to $\phi_f - \phi_b = 45°$, whereas those having positive amplitudes in the mantle correspond to ϕ_f $\phi_b = 135°$. The two black vertical dashed lines show the uniform sensitivity under the assumption of a single vertically incident plane SKS wave, i.e., the SI predicted by $\delta t \sin 2(\phi_f - \phi_b)$. (b) Shear wave speed in the topmost 100 km in model PREM. The two red horizontal dashed lines in Figures 4a and 4b depict the midcrust and Moho discontinuities in PREM.

$$\xi = (S_{\max} + S_{\min}) / \max(|S_{\max}|, |S_{\min}|), \tag{4}$$

where $S_{\max}$ and $S_{\min}$ are, respectively, the maximum and minimum of a given curve. $\xi = 0$ corresponds to a zero-mean curve, while $\xi > 0$ indicates a positive shift, and vice versa. The shifting parameters are shown in Figures 3c and 3d for a suite of epicentral distances and for source depths of 0 km, 20 km and 500 km. The pattern is consistent with what we have seen in Figure 2b: $\xi \approx 0$ in the distance range of ~88°–115° in which the SKS is not significantly affected by the interference with other phases (Figure 3c). For distances less than ~88°, there is a large negative shift caused by a strong interference with the mantle-turning *S* wave which has a very different incidence angle. As seen in the prediction for 85° distance (black solid curve in Figure 3a), not only are there a negative shift in the SI but also a shift in the differential angle $\phi_f - \phi_b$. This implies that if one were to use the SI obtained from an earthquake at an epicentral distance of 85°, there would be biases in both splitting time δt and the azimuth of the fast axis ϕ_f. Beyond ~115° the pattern is more complicated because of contributions from interfering phases such as SPdKS/SKPdS, PcPPcS, and PPPP. The interference effect becomes weaker for deeper sources. For SKKS (Figure 3d), which is also often used to measure shear wave splitting, the interference effect is significant only for very shallow sources at distances less than ~100°.

The predictions in Figures 3a and 3b also show clear discrepancy between the splittings of SKS and SKKS, especially at large epicentral distances. The reason is obvious: the SKS and SKKS are affected at different distances and by different neighboring phases (Figure 2). The SKS-SKKS splitting discrepancy has been observed and interpreted in terms of complex anisotropy in the D" region [e.g., *Long*, 2009]. Our full-wave result suggests that upper-mantle anisotropy can also contribute to SKS-SKKS splitting discrepancy.

The near-field effect can be clearly seen in the SI prediction for $\Delta = 100°$ (red curve in Figure 3a). Although it has nearly zero shift (Figure 3c) owing to stronger SKS wave amplitude relative to other interfering phases, the amplitude of the predicted splitting intensity is very different from the ray-theoretical one (black dashed curve) with a discrepancy of ~0.3 s (~26%) in the estimation of splitting time δt. This is mostly due to the near-field effect and the multiple reflections from near-surface discontinuities as illustrated by the highly concentrated and rapidly oscillating sensitivity (Figures 1b and 1d) in the vicinity of the station. The effect of these full-wave behaviors can also be seen in the depth-varying (i.e., one-dimensional) sensitivities of splitting intensity for γ as shown in Figure 4 obtained by horizontally integrating the 3-D kernels (i.e., the quantity inside the curled bracket in equation (3) assuming a unity γ and ignoring negligible contributions from ε and δ). At depths in the mantle, the 1-D kernels are more or less straight lines with little depth variation. However, they fluctuate wildly near the surface as well as the midcrust and Moho discontinuities as a consequence of the combined effects from a strong near-field complexity and the multiple reflections within the two crustal layers. *Favier and Chevrot* [2003] demonstrated the near-field behavior of the finite-frequency SI kernel. Their result was, however, not fully representative of the SKS wave in a realistic Earth structure, since they assumed a homogeneous half-space velocity model. All the full-wave 1-D kernels for different epicentral distances in Figure 4 show some level of departure from the ray-theoretical kernel (black dashed lines). The full-wave kernel at 100° (red lines) follows the curve of the ray-theoretical kernel most closely in the mantle, but has a much larger value than the ray-theoretical one in the crust. This results in the ~0.3 s discrepancy in the estimation of δt as seen in Figure 3a. Thus, even when SKS wave is well-isolated or dominant relative to its neighboring phases, near-field effect can still have significant contribution to the shear wave splitting intensity. The asymmetry in the 1-D kernels with respect to the vertical axis of $S = 0$ is also consistent with the vertical shifts of the sinusoidal curves in Figure 3a.

4. Conclusion

Using the full-wave sensitivity kernels of SKS splitting intensity to elastic anisotropic parameters calculated by normal-mode theory, we have demonstrated that the interference of SKS with other phases of similar arrival times, the near-field effect, and the multiple reflections in the crust can lead to strong dependence of the splitting intensity on the epicentral distance. The full-wave effects are neglected in the common practices of shear wave splitting analysis which explicitly assumes that the observed SKS or SKKS phase is composed of a single vertically incident plane wave. The adoption of such an assumption simplifies the interpretation of shear wave splitting in terms of the strength of anisotropy and the direction of the fast axis of symmetry. However, this assumption not only imposes a strong restriction on the source-receiver geometry in the application of SKS splitting analysis but also allows only for the characterization of an average (uniform) anisotropic structure in the crust and mantle. The full-wave sensitivity kernels account for the effects of all possible wave interferences involved in shear wave splitting and therefore loosen the restrictions on source-receiver geometry amenable to shear wave splitting analysis. Furthermore, the 3-D Fréchet kernels also afford us the capability to resolve the vertical and lateral variations in seismic anisotropy and obtain 3-D images of the Earth's anisotropic structure.

Acknowledgments
We thank Dr. S. Chevrot and an anonymous reviewer for their constructive comments which helped improve our manuscript. This work has been supported by a Career Development Award of Academia Sinica of Taiwan under Grant AS-98-CDA-M02. All figures except for Figure 1 have been generated by the Generic Mapping Tools of *Wessel and Smith* [1995].

The Editor thanks Sebastien Chevrot and an anonymous reviewer for assisting in the evaluation of this paper.

References

Ando, M. (1984), ScS polarization anisotropy around the Pacific Ocean, *J. Phys. Earth*, *32*, 179–195.
Babuška, V., and M. Cara (1991), *Seismic Anisotropy in the Earth*, Kluwer Academic Publishers, Dordrecht, Netherlands.
Becker, T. W., S. Chevrot, V. Schulte-Pelkum, and D. K. Blackman (2006), Statistical properties of seismic anisotropy predicted by upper mantle geodynamic models, *J. Geophys. Res.*, *111*, B08309, doi:10.1029/2005JB004095.
Browaeys, J., and S. Chevrot (2004), Decomposition of the elastic tensor and geophysical applications, *Geophys. J. Int.*, *159*, 667–678.
Chapman, C. H., J.-Y. Chu, and D. G. Lyness (1988), The WKBJ seismogram algorithm, in *Seismological Algorithms*, edited by D. J. Doornbos, pp. 47–74, Academic Press, London.
Chevrot, S. (2000), Multichannel analysis of shear wave splitting, *J. Geophys. Res.*, *105*, 21,579–21,590.
Chevrot, S. (2006), Finite frequency vectorial tomography: A new method for high resolution imaging of upper mantle anisotropy, *Geophys. J. Int.*, *165*, 641–657.
Crotwell, H. P., T. J. Owens, and J. Ritsema (1999), The TauP Toolkit: Flexible seismic travel-time and ray-path utilities, *Seismol. Res. Lett.*, *70*, 154–160.
Dahlen, F. A., S.-H. Hung, and G. Nolet (2000), Fréchet kernels for finite-frequency traveltimes—I. Theory, *Geophys. J. Int.*, *141*, 157–174.
Dziewonski, A. M., and D. L. Anderson (1981), Preliminary reference Earth model, *Phys. Earth Planet. Int.*, *25*, 297–356.
Favier, N., and S. Chevrot (2003), Sensitivity kernels for shear wave splitting in transverse isotropic media, *Geophys. J. Int.*, *153*, 213–228.
Favier, N., S. Chevrot, and D. Komatitsch (2004), Near-field influences on shear wave splitting and traveltime sensitivity kernels, *Geophys. J. Int.*, *156*, 467–482.
Liu, Q., and J. Tromp (2006), Finite-frequency kernels based upon adjoint methods, *Bull. seismol. Soc. Am.*, *96*, 2383–2397.
Long, M. D. (2009), Complex anisotropy in D″ beneath the eastern Pacific from SKS–SKKS splitting discrepancies, *Earth Planet. Sci. Lett.*, *283*, 181–189.
Mensch, T., and P. Rasolofosaon (1997), Elastic-wave velocities in anisotropic media of arbitrary symmetry-generalization of Thomsen's parameters ε, δ and γ, *Geophys. J. Int.*, *128*, 43–64, doi:10.1111/j.1365-246X.1997.tb04070.x.
Monteiller, V., and S. Chevrot (2011), High-resolution imaging of the deep anisotropic structure of the San Andreas Fault system beneath southern California, *Geophys. J. Int.*, *186*, 418–446.
Savage, M. K. (1999), Seismic anisotropy and mantle deformation: What have we learned from shear wave splitting?, *Rev. Geophys.*, *37*, 65–106.
Sieminski, A., H. Paulssen, J. Trampert, and J. Tromp (2008), Finite-frequency SKS splitting: Measurement and sensitivity kernels, *Bull. seismol. Soc. Am.*, *98*, 1797–1810.
Silver, P. G. (1996), Seismic anisotropy beneath the continents: Probing the depths of geology, *Ann. Rev. Earth Planet. Sci.*, *24*, 385–432.
Silver, P. G., and W. W. Chan (1988), Implications for continental structure and evolution from seismic anisotropy, *Nature*, *335*, 34–39.
Tromp, J., C. Tape, and Q. Liu (2005), Seismic tomography, adjoint methods, time reversal and banana-doughnut kernels, *Geophys. J. Int.*, *160*, 195–216.
Vinnik, L., G. L. Kosarev, and L. I. Makeyeva (1984), Anisotropy of the lithosphere from the observation of *SKS* and, *SKKS*, *Proc. Acad. Sci. USSR*, *278*, 1335–1339.
Wessel, P., and W. H. F. Smith (1995), New version of Generic Mapping Tools released, *Eos Trans. AGU*, *76*, 329.
Wüstefeld, A., G. Bokelmann, C. Zaroli, and G. Barruol (2008), SplitLab: A shear-wave splitting environment in Matlab, *Comp. Geosci.*, *34*, 515–528.
Zhao, L., and S. Chevrot (2011a), An efficient and flexible approach to the calculation of three-dimensional full-wave Fréchet kernels for seismic tomography: I–Theory, *Geophys. J. Int.*, *185*, 922–938.
Zhao, L., and S. Chevrot (2011b), An efficient and flexible approach to the calculation of three-dimensional full-wave Fréchet kernels for seismic tomography: II–Numerical results, *Geophys. J. Int.*, *185*, 939–954.
Zhao, L., and T. H. Jordan (1998), Sensitivity of frequency-dependent traveltimes to laterally heterogeneous, anisotropic Earth structure, *Geophys. J. Int.*, *133*, 683–704.
Zhao, L., T. H. Jordan, and C. H. Chapman (2000), Three-dimensional Fréchet differential kernels for seismic delay times, *Geophys. J. Int.*, *141*, 558–576.